Advances in Water Resources 62 (2013) 1–12

Contents lists available at ScienceDirect

Advances in Water Resources

journal homepage: www.elsevier.com/locate/advwatres

2D and 3D imaging resolution trade-offs in quantifying pore throats for prediction of permeability

L.E. Beckingham [a,1], C.A. Peters [a,*], W. Um [b], K.W. Jones [c], W.B. Lindquist [d]

[a] Princeton University, Princeton, NJ, USA
[b] Pacific Northwest National Laboratory, Richland, WA, USA
[c] Brookhaven National Laboratory, Upton, NY, USA
[d] Stony Brook University, Stony Brook, NY, USA

ARTICLE INFO

Article history:
Received 30 January 2013
Received in revised form 15 August 2013
Accepted 19 August 2013
Available online 3 September 2013

Keywords:
Pore network modeling
Permeability
Mineral precipitation
Hanford
CO_2 sequestration
Alberta sedimentary basin

ABSTRACT

Although the impact of subsurface geochemical reactions on porosity is relatively well understood, changes in permeability remain difficult to estimate. In this work, pore-network modeling was used to predict permeability based on pore- and pore-throat size distributions determined from analysis of 2D scanning electron microscopy (SEM) images of thin sections and 3D X-ray computed microtomography (CMT) data. The analyzed specimens were a Viking sandstone sample from the Alberta sedimentary basin and an experimental column of reacted Hanford sediments. For the column, a decrease in permeability due to mineral precipitation was estimated, but the permeability estimates were dependent on imaging technique and resolution. X-ray CT imaging has the advantage of reconstructing a 3D pore network while 2D SEM imaging can easily analyze sub-grain and intragranular variations in mineralogy. Pore network models informed by analyses of 2D and 3D images at comparable resolutions produced permeability estimates with relatively good agreement. Large discrepancies in predicted permeabilities resulted from small variations in image resolution. Images with resolutions 0.4 to 4 μm predicted permeabilities differing by orders of magnitude. While lower-resolution scans can analyze larger specimens, small pore throats may be missed due to resolution limitations, which in turn overestimates permeability in a pore-network model in which pore-to-pore conductances are statistically assigned. Conversely, high-resolution scans are capable of capturing small pore throats, but if they are not actually flow-conducting predicted permeabilities will be below expected values. In addition, permeability is underestimated due to misinterpreting surface-roughness features as small pore throats. Comparison of permeability predictions with expected and measured permeability values showed that the largest discrepancies resulted from the highest resolution images and the best predictions of permeability will result from images between 2 and 4 μm resolution. To reduce permeability underestimation from analyses of high-resolution images, a resolution threshold between 3 and 15 μm was found to be effective, but it is not known whether this range is applicable beyond the samples studied here.

1. Introduction

Mineral precipitation and dissolution reactions in subsurface porous media may induce changes in porosity and permeability [1–6]. The impact of these reactions on porosity is relatively straightforward, where precipitation reduces porosity and dissolution increases porosity. However, the resulting changes in permeability are much more complex and less understood [7,8]. Specifically, in the case of mineral precipitation, the impact on permeability is dependent on where, within individual pores and a network of pores, precipitation occurs. In some scenarios, precipitation occurs as a relatively uniform coating on grain surfaces as in Crandell et al. [9] (cancrinite coatings on grain surfaces), Luquot et al. [10] (chamosite coatings on grains), Lu et al. [11] (chlorite coatings on quartz grains), while in other cases, precipitation may be related to fluid velocity [12], pore size [13], grain size [8], or mineralogy [14]. Additionally, Crandell et al. [9] surmised that even if precipitation occurs as a uniform coating on grain surfaces, this does not guarantee a uniform effect on flow paths and permeability as some pore throats are closed off due to clogging while others are simply reduced in size.

Predictions of reaction-induced changes in permeability are traditionally based on empirical power law relationships that are related to changes in porosity [15,16]. These relationships predict a single permeability value based on a given change in porosity. However, a single and constant power-law exponent may not

* Corresponding author. Tel.: +1 609 258 5645; fax: +1 609 258 2799.
E-mail address: cap@princeton.edu (C.A. Peters).
[1] Current address: Lawrence Berkeley National Laboratory, Berkeley, CA, USA.

0309-1708/$ - see front matter © 2013 Elsevier Ltd. All rights reserved.
http://dx.doi.org/10.1016/j.advwatres.2013.08.010

universally apply for all porosity changes due to non-uniform structural modifications that may impact permeability in different ways [6,12,17,18]. Recent studies have recognized that both the history and modification path along with the spatial distribution of modifications may impact permeability. Bernabe et al. [17] distinguished between porosity-producing versus porosity-destroying processes and the creation of effective versus non-effective pore space on the porosity–permeability relationships for a porous medium. Gouze and Luquot [5], informed by information from 3D imaging, considered the spatial distribution of alterations of tortuosity and hydraulic radius to explain changes in porosity and permeability.

A research tool to quantify changes in permeability that accounts for changes in flow network topology is to use pore-network models that characterize pore sizes, pore connectivities and pore-throat sizes. The use of pore-network models for reactive transport modeling and to predict permeability began decades ago [19], but it has grown rapidly in the last decade due in part to advances in imaging technologies [12,20–24]. For example, Algive et al. [20] used reactive pore network models to examine the effect of diagenetic cycles on the permeability of carbonate rocks. Reactive pore network models have also been used to consider the evolution of permeability in the context of CO_2 sequestration [6,21,25–28].

Pore network models are often defined by mapping pores on a regular cubic lattice and assigning connections, or pore throats, between pores [6,19–21,23–25,29,30]. The maximum number of connections allowed to a pore, or pore coordination number, has varied between models with the most recent model developed by Raoof and Hassanizadeh [29] allowing for 26 possible connections in 13 different directions. The pore sizes, pore-throat sizes, and network connectivity are statistically assigned by sampling from probability distributions or histograms. Then, flow is numerically simulated and permeability can be inferred. Other methods for pore network construction, as in Kim et al. [30], do not use a regular cubic lattice but instead use 3D direct 1-to-1 network mapping. Simulations from that work yielded comparable results for reaction rates computed using a regular cubic lattice in Li et al. [31]. Work on regular cubic lattices has been justified, as pointed out in Raoof and Hassanizadeh [29], as long as the coordination number distribution of the network is accounted for as found in Arns et al. [32].

To provide accurate permeability predictions using pore-network models requires a good description of the pore network topology [32,33]. These descriptions can be obtained using a variety of 2D and 3D imaging methods. The first use of image-obtained pore-space information to reconstruct a pore network consisted of 2D serial sectioning of samples [34,35]. These methods were widely used [36] and expanded to include imaging of rock sections using laser scanning confocal microscopy [37]. Pore- and throat-size distributions have also been obtained from analysis of 2D scanning electron microscopy (SEM) backscattered electron (BSE) images of thin sections [9]. While 2D imaging has the advantage of being widely accessible in addition to providing rapid information about sub-grain and intragranular variations in mineralogy as in Peters [38], it cannot directly provide information about network connectivity. Some studies have used multiple-point statistics from 2D images to generate realistic 3D networks [39,40]. Alternatively, as in this study, the 2D obtained data can be combined with connectivity information from 3D analyses.

The use of three-dimensional methods to provide pore network characterization has grown extensively in recent years. These methods consist of scanning rock specimens using either synchrotron X-ray computed microtomography (X-ray CMT) [1,41] or benchtop computed tomography (CT) [4,42]. Reviews in Werth et al. [43] and Wildenschild and Sheppard [44] detail the recent uses of X-ray microtomography for porous media characterization as well as reactive and non-reactive fluid transport. A variety of segmentation and interpretation methods have been deployed with varying success as is described in Sezgin and Sankur [45], Dong and Blunt [46], Porter and Wildenschild [47], Bhattad et al. [48], Wildenschild and Sheppard [44], and Jiang et al. [49]. One widely used approach, which is the approach adopted in this analysis, uses an indicator kriging method to achieve image segmentation [50] and interpret pores and their connections from skeletonization using the medial axis transform [51]. Using this method, nodal pore bodies are first characterized along vertices connecting the percolating backbone medial axis. The remainder of the pore space is informed by forming connections between nodal pores. Pore throats are defined at the minimum area of the pore-to-pore connecting channels [52].

While there are many 2D and 3D imaging methods that can be used to determine the pore network structure, there are few comparisons of 2D and 3D imaging with regard to the success of these methods and their corresponding resolutions. One comparison by Caubit et al. [22] compared 3D benchtop CT imaging with a 2D reconstruction of the pore network for a variety of unconsolidated and consolidated samples. Their intent was to determine if pore-network models informed from either of these methods could accurately match measured properties, including permeability. They found that both the 2D and the 3D methods overpredicted permeability. In the 3D method, permeability was overpredicted in part due to the limitation in voxel resolution (3 μm), which caused imprecisions in determining pore-throat sizes. Additionally, they concluded both methods failed to capture small-scale heterogeneities, contributing to the overprediction of permeability. Peng et al. [53] compared the ability of 12.7 μm and 0.35 μm resolution X-ray CMT analyses to characterize a Berea sandstone sample. They found the lower resolution analysis overestimated pore size and pore connectivity and missed small pores. The higher resolution analysis was able to better describe pore sizes in the sample analyzed but was not able to produce a representative pore-size distribution or pore connectivity due to the small sample volume analyzed [53]. While 3D imaging has the advantage of providing 3D information about the pore network structure, it is practically limited to very small sample size for high-resolution analyses [54]. Recent work by Pamukcu and Gualda overcame the trade-off between sample-size and image-resolution to obtain representative crystal size distributions spanning multiple length scales by combining information from higher and lower resolution 3D tomograms of smaller and larger samples, respectively [55]. However, this approach is still practically limited by beam time availability and the requirement of multiple representative specimens.

The overarching goal of this work is to estimate permeability changes due to mineral precipitation using pore-network models statistically informed with different kinds of imaging information. To achieve this requires (1) examining the differences in permeabilities estimated using statistical network data inferred from 2D images and those estimated using 3D image sets, and (2) examining the impact of image resolution and small pores and pore throats on pore-network model-predicted permeability. While several different image resolutions are considered in this study, variations in small pores and pore throats are used as a proxy for further variations in image resolution. In this study, flow permeability was estimated for a sediment-packed experimental column and for a sandstone sample. The column experiment involved precipitation of secondary minerals in Hanford sediments due to reaction with simulated caustic radioactive tank wastes, which was analyzed for the pore space evolution in Cai et al. [1] and Crandell et al. [9]. The sandstone sample is from the Viking formation in the Alberta sedimentary basin in Canada. The mineral distribution of this sample has been investigated using 2D and 3D imaging

methods in Peters [38] and Kim et al. [30], respectively. The pore-network models were created using statistical topological information inferred either from 2D SEM images [9] or from 3D X-ray CMT [1] data for both samples. The results from these two approaches are compared as well as examined in the context of experimental and expected values.

2. Methods

2.1. Samples

The first sample considered in this study is a 3.1 mm × 8.8 cm PEEK column that was packed with 212 to 300 μm diameter Hanford sediment and reacted with simulated tank waste [1]. Details of the column experiment are given in Cai et al. [1]. The second sample is a sandstone identified as "3w4" from the Viking formation in the Alberta sedimentary basin (Canada). Specifics on the 3w4 sandstone sample are detailed in Peters [38].

2.2. Pore-structure analysis

Both samples were scanned using X-ray CMT at the X2B beam line at the National Synchrotron Light Source at Brookhaven National Laboratory. The reactive column sample was scanned before, periodically during, and after reaction to track the evolution of the pore space. The 3D reconstruction of the pore space for the Hanford column experiment is detailed in Cai et al. [1]. As the sandstone was not reacted, a single scan and reconstruction was created and the details of this analysis are given in Kim et al. [30]. To characterize the pore- and pore-throat size distributions as well as connectivities, the reconstructed 3D pore networks were statistically interpreted using 3DMA-Rock [1,30]. This program involves image segmentation by indicator kriging followed by construction of the percolating backbone medial axis. Pore bodies are defined by finding nodal pores at multigrain junctions and the pores that connect them to other nodes [52]. Pore throats are defined at the minimum area along the channel connecting pore bodies together.

2D SEM image analysis of both samples was performed at Princeton University's PRISM Image and Analysis Center using a FEI Quanta 200 FEG Environmental SEM. After the final 3D X-ray CMT scan of the Hanford column, the contents were solidified with epoxy and sectioned as detailed in Crandell et al. [9]. Polished sections of both samples were imaged using 2D SEM imaging in back-scattered electron (BSE) mode. 2D images of the sandstone 3w4 sample, from the analysis detailed in Peters [38], consisted of images at 1.8 μm and between 3 and 4 μm resolution. SEM images of the Hanford column, from Crandell et al. [9], were taken at a resolution of 0.4 μm. From the 2D images, pore-radii and pore-throat size distributions were determined using an erosion–dilation image analysis method. In this method, the pore space is eroded with a circle structural element and then dilated with the same element. A series of erosion–dilation cycles are used with the size of the structural element increasing with each cycle. Pore seed pixels remaining after pore space erosion are equivalent to pores with a diameter greater than the size of the eroding structural element. A pore throat is defined when a large pore space is divided into two separate pore bodies with the size of the pore throat equivalent to the size of the current structural element. The inherent biases that arise when inferring diameters from 2D images were corrected using sample-specific bias correction values based on principles first developed in stereology, as described in Crandell et al. [9].

2D imaging is not traditionally used to determine changes in the pore network resulting from secondary minerals due to the destructive nature of sample preparation that requires epoxy impregnation and sample sectioning and polishing. This work takes advantage of the method developed in Crandell et al. [9] which digitally alters SEM images to remove secondary mineral precipitates, effectively creating an image of the pore structure before precipitation. Direct comparison of the unaltered pore structure (with secondary minerals present) and the simulated before-precipitation structure allow for analysis of the impact of secondary minerals on the pore network. Note, however, that changes in pore structure due to mineral dissolution cannot be accounted for due to the destructive nature of sample preparation required for 2D imaging.

2.3. Experimental permeability measurement

The permeability of sandstone sample 3w4 was experimentally measured by Core Laboratories (Houston, TX) using a pressure-decay profile permeameter [56]. A total of eight permeability measurements were made on the sandstone core sample. Reference to these experimentally measured values is to the entire range of measured values as opposed to an average of the eight values.

2.4. Pore-network model construction

Pore-network models were created based on the model developed in Raoof and Hassanizadeh [29] in which pores are defined on a regular, square lattice and their sizes randomly assigned from pore-radii distributions (Fig 1.). For this work, the model was constructed of 1000 pores in a 10 × 10 × 10 network corresponding to approximately a 2 mm cube. No-flow boundaries were applied in two directions to create a 1D flow system with fixed fluid pressures at the inlet and outlet of the flow direction. As permeability is an intrinsic property of the medium, it depends solely on the properties of the medium and does not vary with fluid velocity [57]. This was confirmed in the pore-network model by applying different values of boundary fluid pressures, and therefore fluid velocities, and verifying consistent pore-network model-predicted permeability values.

The model developed by Raoof and Hassanizadeh [29] is unique in that it allows for 26 possible connections for each pore. In our model, the number of connections for each pore is related to the pore size, as determined from the 3DMA rock analysis and reported in Cai et al. [1] for the reactive Hanford column experiment and in Kim et al. [30] for sandstone 3w4. To prevent dead-end pores, which do not conduct flow and contribute to permeability, each pore was assigned to have, at a minimum, two connections. This effectively defines the minimum pore size included in the model to a radius of 27 μm and 18 μm for the respective reacted and unreacted Hanford column images [1] and 5 μm for the sandstone [30]. While the correlation between pore size and coordination number was retained from the 3D network, the connection direction was randomly assigned from one of the possible 13 forward directions. The size of each pore throat, or connection, was randomly sampled from the 2D- or 3D-determined pore-throat size distributions. The random sampling of pore and pore-throat sizes did create slight variations in bulk properties, such as porosity, but this effect is expected to be minimal.

2.5. Upscaled permeability prediction

Pore-network models are used to predict permeability by using principles of upscaling, outlined in Li et al. [31] and described below. At the pore scale, for an incompressible fluid and constant pore volume of pore i, the sum of all pore inflows must equal all outflows or,

$$\sum_{j=1}^{nc} Q_{ij} = 0 \tag{1}$$

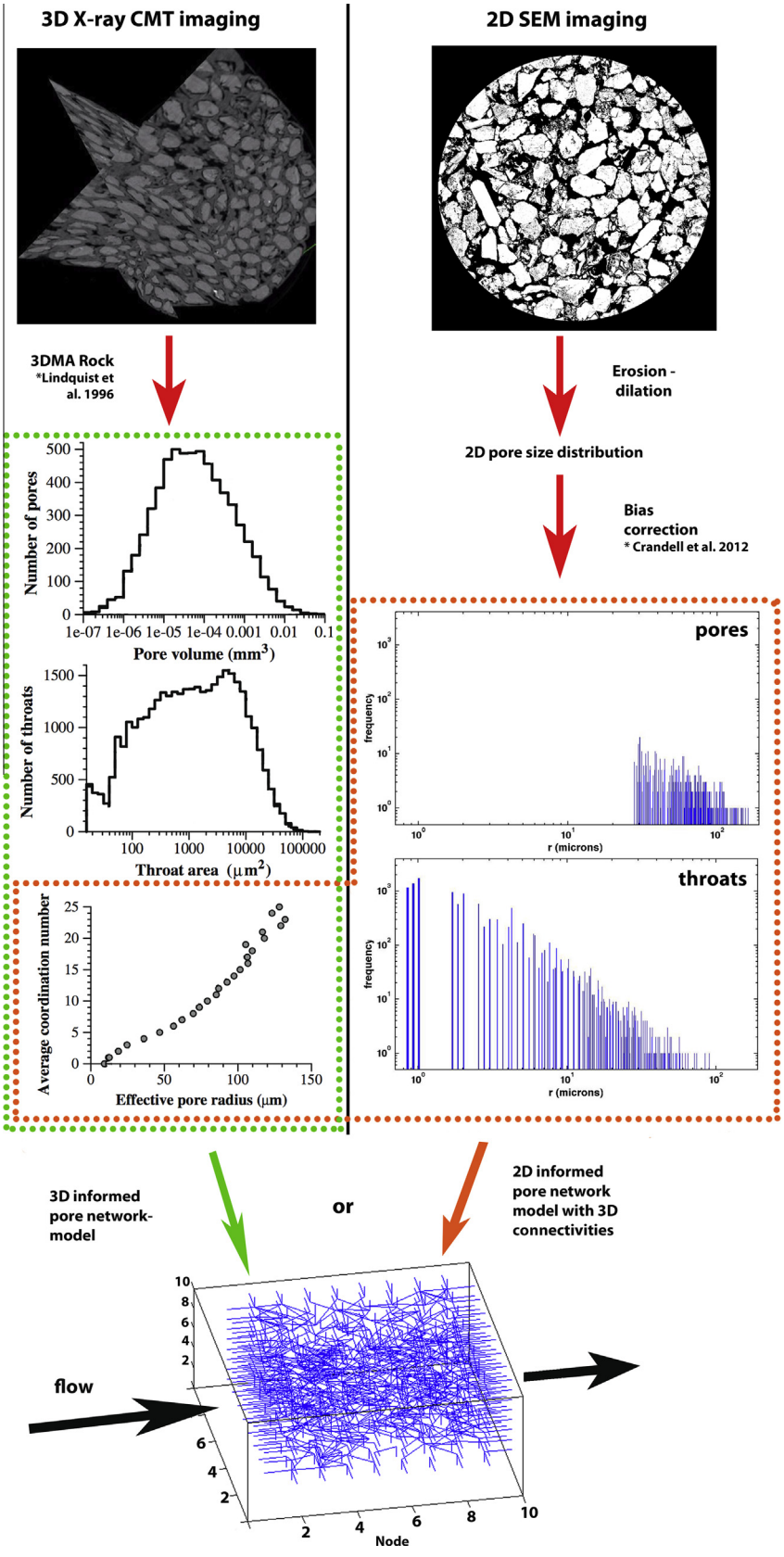

Fig. 1. Conceptualization of the process of informing pore-network models with information from 3D X-ray CMT or 2D SEM imaging.

where nc is the number of connections to and from pore i and Q_{ij} the flowrate from pore i to pore j [31]. The flowrate between pores i and j is proportional to the pressure differential as given by,

$$Q_{ij} = C_{ij}(P_i - P_j) \quad (2)$$

where P_i and P_j are the fluid pressures in pores i and j and C_{ij} is the conductance [31]. Following the method of Li et al. [31], the conductance is related to the diameter of the throat connecting pores i and j, d_{ij}, fluid viscosity v, and pore-throat length l using Poiseuille's law,

$$C_{ij} = \frac{\pi d_{ij}^4}{128 v l} \quad (3)$$

assuming each pore throat can be approximated as cylindrical. Eqs. (1)–(3) are applied at the pore scale and used to calculate the pressure in each node. At the continuum scale, the permeability, K, is computed by applying Darcy's Law,

$$K = \frac{Q_T v L}{\Delta P \Lambda} \quad (4)$$

where Q_T is the total flow rate through the network, L is the length of the network, ΔP the pressure difference between the inlet and outlet boundaries, and Λ the cross sectional area of the pore network perpendicular to the direction of flow.

2.6. Predicted permeability distributions

Because a 1000-node 2 mm^3 is a small system, we applied a statistical approach to examine variability from different manifestations, or variations in value and distribution of sampled pore and pore-throat sizes, of such network systems. For each sample, for both the 2D and 3D pore-radii and pore-throat size distributions, a distribution of pore-network model-predicted permeabilities was compiled by creating one thousand pore-network models with pores and pore throats sampled from the image-derived distributions. For each pore-network model, the permeability was predicted as described above, applying the same boundary conditions and model parameters. To test the sensitivity of pore-network model-predicted permeability to image resolution and small pores and pore throats, a series of analyses were developed.

2.6.1. Sensitivity to 2D image resolution

The sensitivity to 2D image resolution is determined in this study using the 3w4 sandstone sample analysis. Pore-network models were generated from pore- and pore-throat size distributions determined from two different resolutions of SEM images, 1.8 μm and 3 to 4 μm as shown in Fig. 2. These models included all pore throats and pores with a minimum connectivity of 2, corresponding to a pore radius greater than 5 μm. The 2D pore-network model-predicted permeability distributions are then compared with the experimentally-measured permeability to determine the variation in permeability with image resolution.

2.6.2. 2D versus 3D image data

A direct comparison between the 2D and 3D methods for generating statistical pore information was performed through analysis of the sandstone sample. A 4 μm resolution 3D-predicted distribution is compared with a 3 to 4 μm resolution distribution determined from the 2D analysis. At essentially the same resolution, this analysis allows for examination of the effect of using 2D or 3D methods to characterize the pore space for pore-network models.

2.6.3. Sensitivity to small pore throats in 2D images

The third analysis tested the sensitivity of permeability predicted from the pore-network model to the abundance of small pore throats as a proxy for variation in image resolution. Pore-throat size distributions from 2D image analysis of the Hanford column were truncated to apply a threshold that specified the minimum size for flow-conducting pore throats, or a pore-throat threshold. The lower-size bound for flow-conducting pore throats was varied in 1 μm intervals from 1 to 5 μm. As in the original pore-network models, these pore-network models included all flow-conducting pores, or those with a minimum connectivity of 2 for each pore. For the Hanford column this corresponds to a smallest pore radius of 27 μm. Highlighted in Fig. 3 are the truncated pore-throat size distributions for each of the pore-throat threshold tests. As above, a distribution of predicted permeabilities was computed for each threshold value by creating one thousand pore-network models from each distribution.

2.6.4. Sensitivity to pore size and coordination in 2D images

This analysis was designed to examine the sensitivity of pore-network model-predicted permeability to abundance of the smallest pore sizes, which also affects the pore network by altering the pore coordination numbers. This series of analyses involved truncations to increase the smallest pore radii to 27, 30, 35, 40, 45, and 50 μm in the Hanford column 2D pore-size distribution. Fig. 3(B) shows the pore-radii distributions corresponding to each test. As the coordination number is related to the pore size as described above, increasing the smallest pore radii increases the corresponding smallest coordination number from 2 to 4. No change was made to the pore-throat distribution and the original 2D distribution corresponding to a resolution of 0.4 μm was used.

2.6.5. Predictions of precipitation induced changes in permeability

The final analysis aims to predict mineral precipitation induced changes in permeability using pore-network models informed with both 2D and 3D distributions. As the Hanford column was scanned using 3D X-ray CMT both before and after reaction, pore- and pore-throat size distributions as well as corresponding coordination data were determined. Digitally-created pre-precipitation 2D images (see Section 2.2 and [9]) were analyzed to determine the before-precipitation pore- and throat-size distributions. These distributions were used to generate pore-network models and corresponding distributions of pore-network model-predicted permeabilities that were compared with calculations of final permeability. In addition, the impact of applying a constant pore-throat threshold, determined in the third analysis, to both before- and after- reaction pore-throat distributions was examined.

3. Results and discussion

3.1. Hanford column experiment

3.1.1. Permeability predicted from 2D image data

The distribution of predicted permeabilities for the reacted Hanford column computed from the pore- and pore-throat size distributions from the 2D image analyses is shown in Fig. 4 (labeled 2D 0.4 μm resolution). The distribution shows a range of permeabilities from 6×10^{-17} to 7×10^{-16} m^2 (6×10^{-5} to 7×10^{-4} D), capturing the variability in possible outcomes for 1000 versions of network models informed from the same pore- and pore-throat size distributions. The total number of nodes (1000) was selected to remain representative while maintaining a reasonable computational time. We tested the representativeness by increasing the total number of network nodes and found that if each network had been larger than 1000 nodes, the variability in permeability estimates was tighter but had the same central tendency.

Ideally, we would compare these estimates with an experimentally-measured permeability for the column, but one could not be

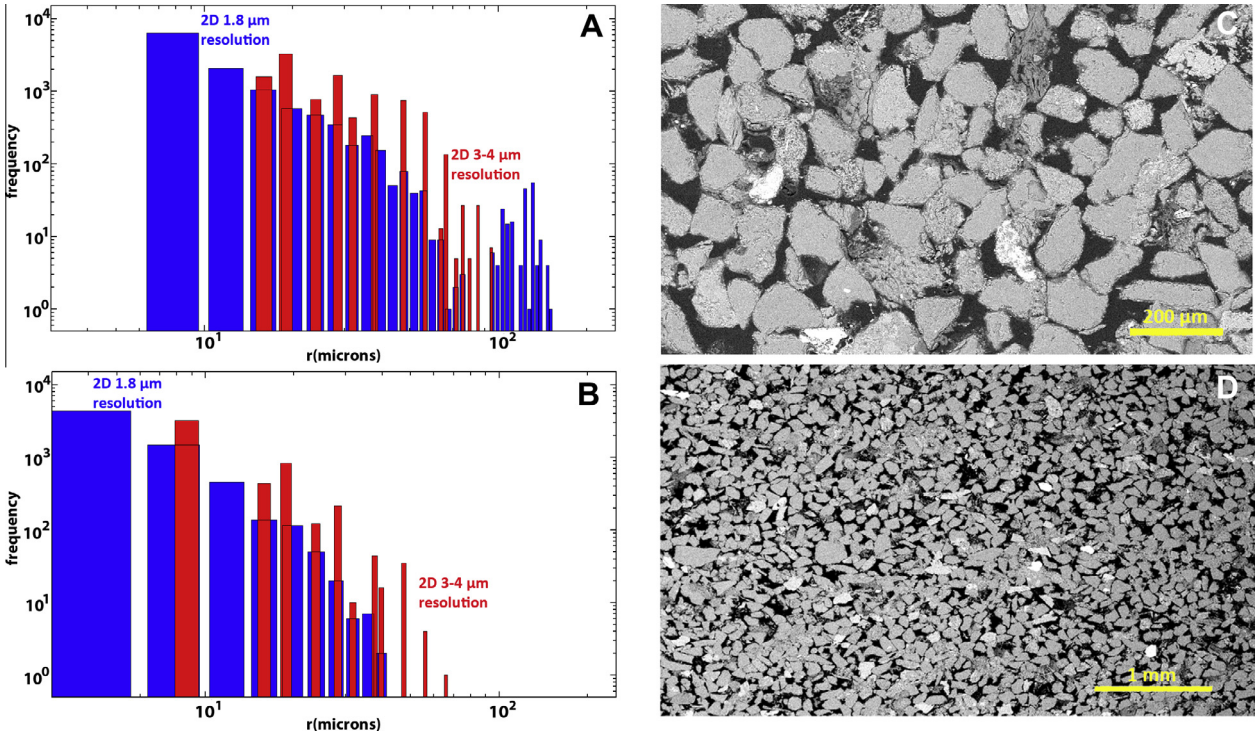

Fig. 2. Pore- (A) and pore-throat size (B) distributions for sandstone sample 3w4 as determined from 1.8 μm (C) and 3 to 4 μm (D) resolution 2D SEM images.

determined for a variety of reasons. However, for unconsolidated fine-grain sands, the expected permeability range is 10^{-14} to 10^{-11} m^2 (10^{-2} to 10 D) [58]. This range is reasonable for the unreacted sands. After reaction, mineral precipitation on grain surfaces decreased pore and pore-throat sizes and cemented some of the grains together, thereby clogging some pore throats [9]. Therefore, the permeability of the reacted column should be lower. We may reasonably expect the final permeability for the reacted column to be a few orders-of-magnitude lower, such as 10^{-15} to 10^{-12} m^2 (10^{-3} to 1 D). The expected permeability of the column was also calculated using the Kozeny–Carman equation,

$$K = B\frac{\phi^2}{(1-\phi)^2}d^2 \tag{5}$$

where B is a geometric factor of 3/2, d the average grain diameter, and ϕ the porosity [15,16,59]. An average grain diameter of 250 μm [1] and porosity values from both the 2D- and 3D-image analysis in Crandell et al. [9] were used to calculate column permeabilities of 6.7×10^{-12} m^2 (6.7 D) and $4.1\text{x}10^{-12}$ m^2 (4.1 D), respectively. These permeability values calculated from the Kozeny–Carman relationship agree well with the above-mentioned range.

The entire range of pore-network model-predicted permeability values from the 2D image analysis of the reacted column are much smaller than those expected based on grain type and computed from the Kozeny–Carman, by as much as 4 orders-of-magnitude. This underestimation is because of the high abundance of small pore throats in the distribution used to populate the network models. We speculate that some of the small pore throats do not conduct flow or are actually surface-roughness features (Fig. 5) that are misinterpreted as small flow-conducting pore throats and to accurately predict permeability using pore-network models from the 2D distributions requires defining a pore-throat threshold for flow-conducting pore throats.

3.1.2. Permeability predicted from 3D image data

Permeabilities predicted for the reacted Hanford column from the pore- and pore-throat size distributions resulting from 3D image analysis range from 10^{-12} to 10^{-11} m^2 (1 to 10 D) (Fig. 4 labeled with 3D 4 μm resolution). These permeabilities are slightly larger than the Kozeny–Carman calculated post-reaction permeability. This is likely due to limitations in voxel resolution which will cause small pores and pore throats to be missed. For a pore-network model constructed from statistically-populated parameters, this will result in overestimation of permeability.

3.1.3. 2D- versus 3D-predicted permeability and sensitivity to image resolution

As shown in Fig. 4, for the reacted Hanford column there is a huge discrepancy between the permeabilities predicted from the 2D and 3D pore- and pore-throat size distributions (labeled with 2D 0.4 μm resolution and 3D 4 μm resolution). We do not believe this is an artifact of trying to determine distributions from 2D images as there is a relatively good agreement between pore-network model permeability predictions for the sandstone sample from 2D and 3D image data of similar resolution (as presented in Section 3.2.3). The resolution of the 2D images is 0.4 μm, and, as stated above, may result in the misinterpretation of surface-roughness features as small pore throats or require thresholding to separate flow- from non-flow conducting small pore throats. Conversely, the voxel resolution of the 3D image data is 4 μm, which will cause small pore throats to be missed, especially those at grain-to-grain boundaries. Despite only a one order-of-magnitude difference in image resolution, the predicted permeabilities are more than four orders-of-magnitude different. The series of analyses further examines the impact of image resolution on pore-network model-predicted permeability and subsequently the impact of underestimating or overestimating small pores and pore throats.

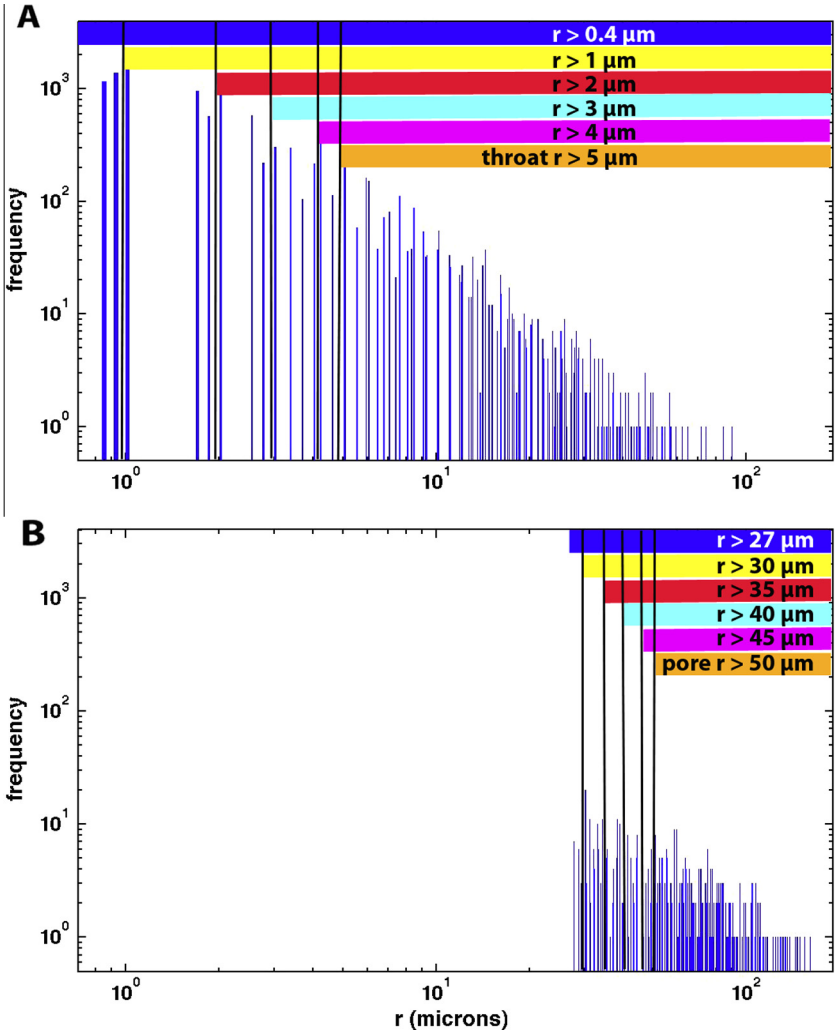

Fig. 3. Pore- (B) and pore-throat (A) size distributions for Hanford column determined from 0.4 µm resolution 2D SEM images. Horizontal bars reflect the portion of the pore- or pore-throat distribution included in the thresholding analyses that vary the smallest pore and pore-throat radii included in the pore network model.

3.2. Sandstone sample 3w4

3.2.1. Permeability predicted from 2D image data

The permeability for sandstone 3w4 was predicted using pore-network models informed from two resolutions of 2D images as shown in Fig. 6. For the 1.8 µm resolution images, permeability predicted from pore-network modeling ranged from 2×10^{-15} to 2×10^{-14} m^2 (2×10^{-3} to 2×10^{-2} D). The permeability range predicted from the pore-network model informed by the 3 to 4 µm resolution 2D images is much higher, spanning 2×10^{-13} to 8×10^{-13} m^2 (0.2 to 0.8 D). Also shown in Fig. 6 is the range of experimentally-measured permeability values for sandstone 3w4. In comparison, permeabilities predicted from the pore-network modeling informed from the 1.8 µm resolution 2D images are much smaller, by up to two orders-of-magnitude. Permeability values predicted from pore-network models informed from 3 to 4 µm resolution images agree relatively well with the experimentally-measured values. This suggests that the 1.8 µm resolution images misinterpret small pore throats and require thresholding to separate flow-conducting pore throats from other small pore throats or surface-roughness features, a concept that is further explored in the series of analyses to follow.

3.2.2. Permeability predicted from 3D image data

As is also shown in Fig. 6, permeability predicted from the pore-network model using the 3D-determined pore- and pore-throat size distributions for the sandstone sample 3w4 range from 5×10^{-13} to 2×10^{-12} m^2 (0.5 to 2 D). These permeability predictions are slightly larger than the experimentally-measured values, within one order-of-magnitude. Voxel resolution limitations, as postulated above, are likely underestimating small flow-conducting pore throats resulting in overestimating predicted permeability. This projection is consistent with the results present in Caubit et al. [22] who observed X-ray CMT voxel limitations led to overestimations of predicted permeability.

3.2.3. 2D- versus 3D-predicted permeability and sensitivity to image resolution

As observed for the Hanford column analysis above, small differences (microns) in 2D versus 3D image resolution resulted in a large difference (orders of magnitude) in pore- network model permeability predictions. The analysis for the 3w4 sandstone, however, has the advantage of being able to compare similar resolutions in 2D and 3D as well as compare pore-network model-predicted permeabilities with experimental values. Predicted permeabilities from the pore-network models informed from 2D and 3D imaging data with comparable resolution agree relatively well (Fig. 6). The permeability predictions from the pore-network model based on 2D images at 3 to 4 µm resolution have a slightly lower range of permeability values predicted. This is likely because their slightly higher (up to 1 µm) resolution captures some smaller pore throats missed in the 3D analysis. While both the 2D and 3D

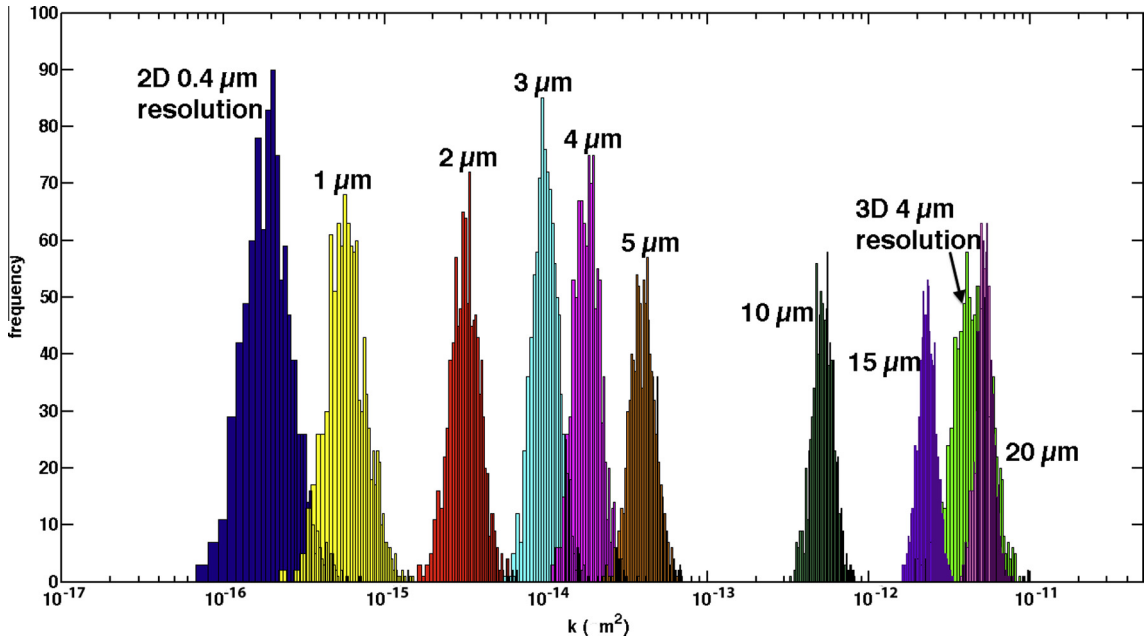

Fig. 4. Distributions of pore-network model-predicted permeabilities for the reacted Hanford column from 3D images (at 4 μm resolution) and from 2D images with increasing pore-throat threshold (indicated above the distribution).

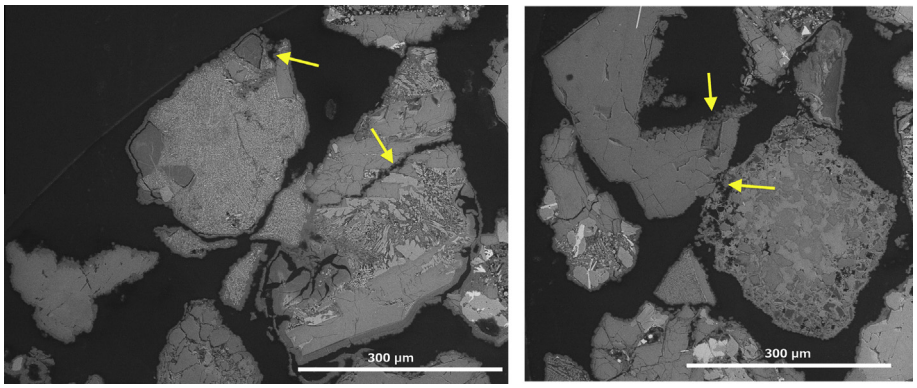

Fig. 5. SEM BSE images of reacted Hanford sediment where surface roughness features create small pores and pore throats.

~4 μm resolution pore-network model permeability predictions agree relatively well with the experimentally-measured values, there is better agreement with the slightly better resolution (3 to 4 μm) 2D predictions. This suggests that a resolution of 4 μm is slightly too coarse to completely capture all permeability controlling features. In addition, this analysis shows a resolution of 1.8 μm overestimates small features. The ideal resolution for the sandstone sample would fall between 1.8 μm and 4 μm, closer to 4 μm than 1.8 μm. This may also be the ideal image resolution range for the column sample as a similar relative agreement between the 4 μm pore-network model-predicted and Kozeny–Carman computed permeability values was observed.

3.3. Further analyses

3.3.1. Sensitivity to small pore throats in 2D images

As the pore-throat threshold for the 2D Hanford reacted column images was increased from 0.4 μm to 1, 2, 3, 4, and 5 μm, the pore-network model-predicted permeabilities increased by up to three orders-of-magnitude as shown in Fig. 4. The difference between two pore-network model-predicted permeability distributions decreases as the size of the smallest pore throat increases. For example, there is less difference between the pore-network model-predicted distributions from smallest pore throats with radii of 4 μm and 5 μm than there is between distributions predicted with smallest pore throats of 1 μm and 2 μm. This suggests that the smaller the pore-throat size, the larger effect it has on decreasing pore-network model-predicted permeability.

While the differences between pore-throat thresholds are small, a maximum of 1 μm, their impact on pore-network model-predicted permeability is large, up to three orders-of-magnitude. Small increases (microns) in the smallest flow-conducting pore-throat size have huge impacts on pore-network model-predicted permeability because of the high abundance of small pore throats in the 2D distributions. As the pore-throat threshold is increased, many small pores are removed from the sampling distribution. Decreasing the total number of small pore throats reduces the proportion of small pore throats to total pore throats. This results in a higher fraction of flow-through larger pore throats in the network, increasing pore-network model-predicted permeability. Additionally, as the threshold is increased, the smallest pore throat included in the model increases in size, which increases predicted permeability.

In comparison with the expected permeability of the reacted column, computed above from the Kozeny–Carman relationship,

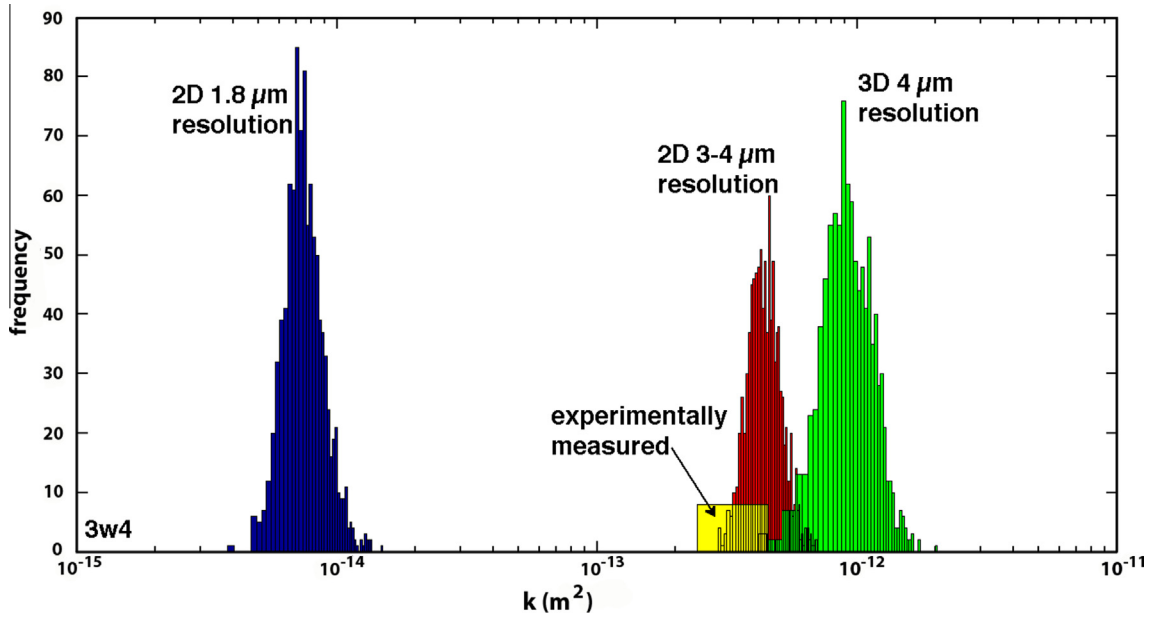

Fig. 6. Distributions of pore-network model-predicted permeability for sandstone sample 3w4 from 2D images of two different resolutions, 3D image analysis, and experimentally-measured permeability.

a large flow conducting pore throat threshold was required to predict permeability from the pore-network model. The Kozeny–Carman computed column permeability, as calculated in Section 3.1.1, is approximately 4 to 7 $\times 10^{-12}$ m^2 (4 to 7 D). To reach this Kozeny–Carman computed permeability, a pore-throat threshold between 10 μm and 15 μm was required. This suggests that the high resolution 2D pore-throat distribution is overestimating small flow-conducting pore throats as it required removing all pore throats with a radii less than at least 10 μm to predict the permeability from the pore-network model that was computed from the Kozeny–Carman relationship for the column.

3.3.2. Sensitivity to small pores in 2D images

The smallest pore in the original Hanford column 2D distribution had a radius of 27 μm, set to correspond to a minimum connectivity of 2. As the size of the smallest pore included in the pore network was increased up to a radius of 50 μm, there was relatively little change in the pore-network model-predicted permeability distributions (see Fig. 7). The distributions that include all flow-conducting pores and those with a minimum pore radii of 50 μm are only slightly different and even have some overlapping permeability predictions. In fact, for all pore radii tested, the pore-network model-predicted permeability distributions overlap the original permeability predictions for the unaltered 2D distributions. This shows that the pore-network model-predicted permeability is not very sensitive to the smallest pore radii.

In comparison with changing the smallest pore throats, as in the last analysis, the sensitivity of pore-network model-predicted permeability to smallest pores is small. The minimum pore radius was increased by 23 μm while in the previous analysis, the smallest pore-throat size was effectively increased by 4.6 μm. Despite that the increase in minimum pore radius in this analysis was five times greater than the increase in pore-throat size in the last analysis, the differences in the pore-network model-predicted permeability distributions are substantially less. This is further evidence that the pore-network model-predicted permeability is much more sensitive to changes in pore-throat sizes than pore radius and evidence that the smallest pore throats control the permeability if it is predicted from a statistically-sampled pore-network model.

3.3.3. Predictions of precipitation-induced changes in permeability

The Hanford column permeability predicted from the pore-network model informed from the 2D before-reaction images, i.e. those with precipitation digitally removed, ranged from 6×10^{-14} m^2 to 6×10^{-15} m^2 (6×10^{-2} to 6×10^{-3} D) as shown in Fig. 8. In comparison with the permeability predicted from the pore-network model based on the reacted 2D SEM images of the column, precipitation caused a decrease in permeability of up to two orders-of-magnitude. However, as stated in Section 3.1.1, the expected permeability range for the unreacted sediment is 10^{-14} to 10^{-11} m^2 (10^{-2} and 10 D) and the Kozeny–Carman computed permeability for the column before reaction is 1.8×10^{-11} m^2 (18 D) and 6.3×10^{-12} m^2 (6.3 D) for the 2D and 3D analyses, respectively. Thus, as was true with the unaltered images, pore-network model-predicted permeabilities from the digitally-altered images is lower than the expected column permeability. Again, the high-resolution 2D images underpredict permeability by overestimating small pore throats.

To accurately predict permeability of the column, a pore-throat threshold of 10 to 15 μm needs to be applied. Applying a pore-throat threshold of 15 μm to the before-reaction pore-throat distribution predicts permeabilities between approximately 3×10^{-12} m^2 and 8×10^{-12} m^2 (3 to 8 D) which is in good agreement with the Kozeny–Carman computed permeability. Comparing the thresholded before- and after- pore-network model-predicted permeabilities shows a much smaller reaction-induced decrease in permeability, within an order-of-magnitude.

4. Conclusions

We showed that permeabilities predicted from statistically-informed pore-network models were very different depending on the images that were used to determine the probability distributions of pore-throat sizes. In the Hanford column experiment, a one order-of-magnitude difference in image resolution resulted in over four orders-of-magnitude difference in pore-network model-predicted permeability. While the experimental permeability for this column was not known, based on Kozeny–Carman approximations we speculate that the column permeability was between

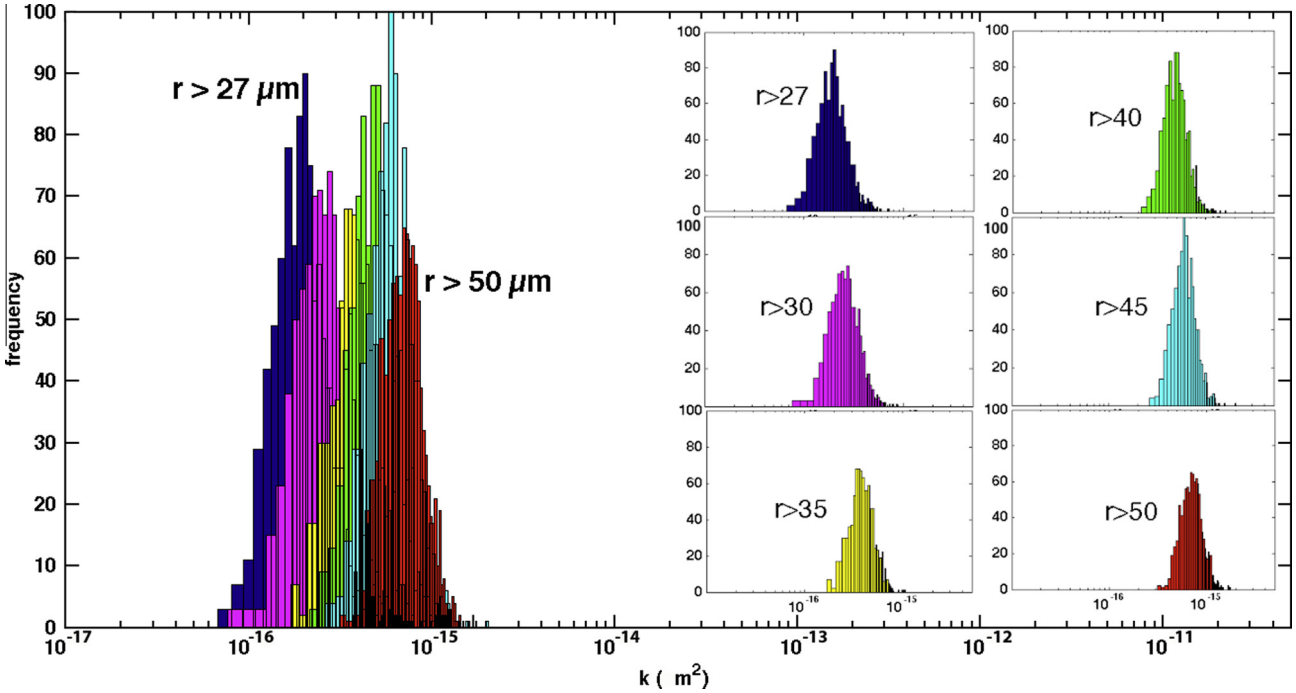

Fig. 7. Distributions of pore-network model-predicted permeabilities for the Hanford reacted column from 2D 0.4 μm resolution images with varying smallest sizes for the pore-size distributions of 27, 30, 35, 40, 45, and 50 μm.

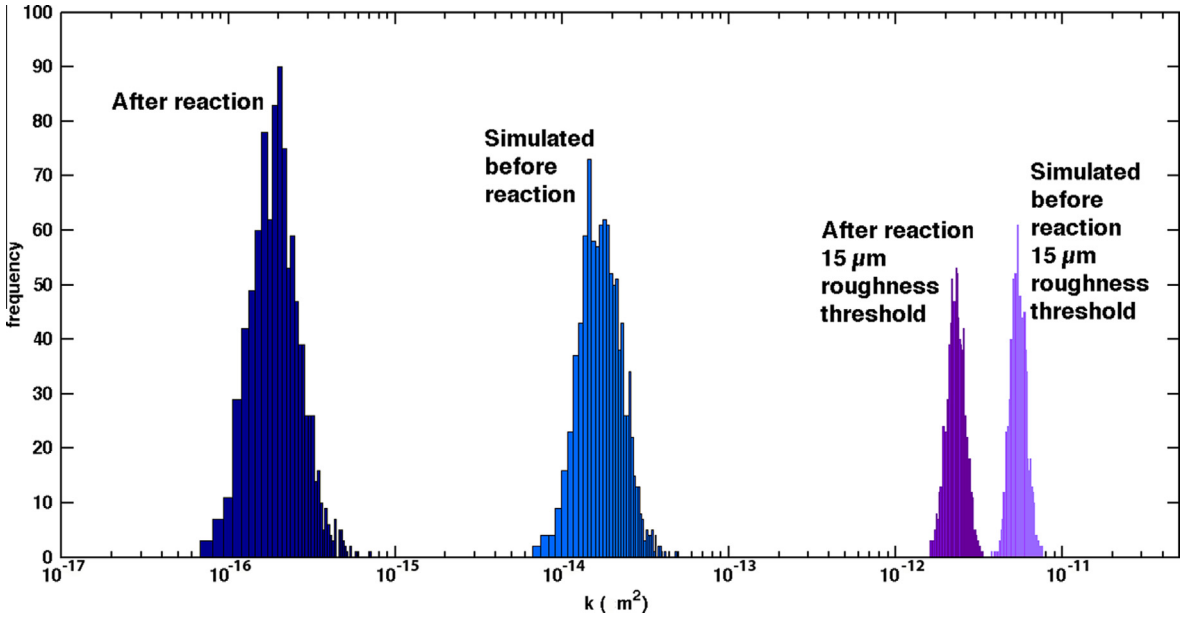

Fig. 8. Distributions of pore-network model-predicted permeabilities for the Hanford reacted column and before-reaction column from 2D image analyses (with no pore-throat threshold). Also shown are permeabilities before- and after-reaction predicted from 2D pore-throat distributions with a pore-throat threshold, or minimum flow-conducting pore-throat size, of 15 μm.

these two endpoints. That is, the high-resolution 2D image analysis resulted in underestimation of the permeability and the lower-resolution 3D image analysis resulted in slight overestimation of the permeability. For the 3w4 sandstone sample, there was a relatively good agreement between the experimentally-measured permeability and that predicted by the pore-network model informed by information from 2D images with resolution of 3 to 4 μm. However, there was a huge discrepancy when predictions were based on 2D images with the highest resolution, 1.8 μm.

Collectively, this suggests that at high resolution, porosity features are misinterpreted as permeability-controlling features, and at low resolution, important permeability-controlling features may be missed. This is in agreement with prior work by Caubit et al. who found limitations in X-ray CMT voxel resolutions missed some important small-scale features resulting in over-estimating permeability values [22]. The analyses presented in the sections above also revealed that 2D and 3D analysis at comparable resolutions may result in relatively equivalent predictions of

permeability, as was the case for the sandstone sample. This suggests that the discrepancy in pore-network model-predicted permeability is not a result of 2D versus 3D image analysis, but a result of differences in image resolution. This was examined in a series of analyses designed to explore the sensitivity of permeability predictions to image resolution. For the 2D images, the resulting pore-throat size distributions were thresholded, which served as a proxy to reducing the resolution of the 2D image as the size of the smallest features captured would increase as resolution was decreased. Contrary to what was expected, for the Hanford column case, a 4 μm thresholded 2D image is not equivalent to a 4 μm resolution 3D image set in terms of pore-throat size distribution and the resulting pore-network model permeability prediction. A resolution threshold of 15 μm was needed to match the pore-network model permeability prediction from the 3D image analysis. As pointed out in Caubit et al. [22], decreasing the image resolution also introduces imprecisions in determining the pore and pore-throat sizes. Therefore, the discrepancy between the 2D 4 μm thresholded predictions and the 3D 4 μm predictions may be due to the combined effects of missing small pores and pore throats and imprecisions in pore and pore-throat sizes.

This work has shown that the permeability predicted by pore-network modeling is controlled by the smallest pore-throat size and is not very sensitive to changes in small pores. It is therefore necessary that small pore throats are accurately determined from the imaging and analysis method. In terms of predicting the effects of geochemical reactions, small changes in pore-throat size due to mineral precipitation or dissolution may result in large changes in permeability. It is most important to understand how mineral dissolution and precipitation reactions alter the smallest pore throats to predict the corresponding changes in permeability. It is also worth noting that several other bulk rock properties beyond single-phase permeability may be affected by variation in small pore-throat sizes as well but these effects are not considered here.

Much of the analysis presented in this paper focused on 2D images because this enabled an investigation of the effects of fine image resolution. However, it remains the case that 3D imaging is essential for informing pore-network models because the only way to characterize pore-network structure and pore connectivity is from 3D imaging. Nonetheless, the findings from this work have important implications for interpretation of 3D scans, as it is inevitable that as imaging technologies improve, the resolution capabilities of 3D imaging will improve as well. While we are inclined to favor increasingly higher resolutions as superior, we demonstrated that a higher image resolution does not necessarily improve permeability predictions. In fact, a higher image resolution may actually underestimate permeabilities. This underestimation may be a result of misinterpreting flow-conducting small pore throats or misinterpreting surface-roughness features as small pore throats. To separate no-flow small pore throats from flow-conducting pore throats would require selecting a threshold for the minimum flow-conducting pore-throat size. However, in statistically-based pore-network models, predicted permeabilities are highly sensitive to the smallest pore throats and selecting a pore-throat threshold a priori is not a trivial matter as small changes in the threshold can result in order-of-magnitude changes in predicted permeability. For the samples studied here, a resolution threshold between 3 and 15 μm was effective in accurate permeability prediction, but more work would need to be done to determine if these results are applicable beyond these samples.

Acknowledgements

This material is based upon work supported by the Department of Energy under Award Numbers DE-FG02-09ER64747 (SUNY Stony Brook); DE-FG02-09ER64748 (Princeton University); and KP1702030-54908 (Pacific Northwest National Laboratory). The information does not necessarily reflect the opinion or policy of the federal government and no official endorsement should be inferred. Use of the National Synchrotron Light Source, Brookhaven National Laboratory, was supported by the U.S. Department of Energy, Office of Science, Office of Basic Energy Sciences, under Contract No. DE-AC02-98CH10886. We also acknowledge the use of PRISM Imaging and Analysis Center, which is supported in part by the NSF MRSEC program through the Princeton Center for Complex Materials (Grant DMR-0819860).

References

[1] Cai R, Lindquist WB, Um W, Jones KW. Tomographic analysis of reactive flow induced pore structure changes in column experiments. Adv Water Resour 2009;32:1396–403.
[2] Emmanuel S, Berkowitz B. Mixing-induced precipitation and porosity evolution in porous media. Adv Water Resour 2005;28:337–44.
[3] Colon CFJ, Oelkers EH, Schott J. Experimental investigation of the effect of dissolution on sandstone permeability, porosity, and reactive surface area. Geochim Cosmochim Acta 2004;68:805–17.
[4] Um W, Serne RJ, Yabusaki SB, Owen AT. Enhanced radionuclide immobilization and flow path modifications by dissolution and secondary precipitates. J Environ Qual 2005;34:1404–14.
[5] Gouze P, Luquot L. X-ray microtomography characterization of porosity, permeability, and reactive surface changes during dissolution. J Contam Hydrol 2011:45–55.
[6] Nogues JP, Fitts JP, Celia MA, Peters CA. Permeability evolution due to dissolution and precipitation of carbonates using reactive transport modeling in pore networks. Water Resour Res 2013, in press. http://dx.doi.org/10.1002/wrcr.20486.
[7] Gouze P, Hassani R, Bernard D, Coudrain-Ribstein A. Computing permeability change in sedimentary reservoirs including clays: application to the Bray fault zone (Paris Basin). Bull Soc Geol France 2001;172:427–36.
[8] Tenthorey E, Scholz CH. Mapping secondary mineral formation in porous media using heavy metal tracers. J Geophys Res 2002;107.
[9] Crandell LE, Peters CA, Um W, Jones KW, Lindquist WB. Changes in the pore network structure of Hanford sediments after reaction with caustic tank wastes. J Contam Hydrol 2012:89–99.
[10] Luquot L, Andreani M, Gouze P, Camps P. CO_2 percolation experiment through chlorite/zeolite-rich sandstone (Pretty Hill Formation – Otway Basin – Australia). Chem Geol 2012;294–295:75–88.
[11] Lu J, Kharaka YK, Thordson JJ, Horita J, Karamalidis A, Griffith C, et al. CO_2-rock-brine interactions in Lower Tuscaloosa Formation at Cranfield CO_2 sequestration site, Mississippi, USA. Chem Geol 2012;291:269–71.
[12] Algive L, Bekri S, Vizika O. Pore-network modeling dedicated to the determination of the petrophysical-property changes in the presence of reactive fluid. SPE J 2010;15:618–33.
[13] Emmanuel S, Ague JJ, Walderhaug O. Interfacial energy effects and the evolution of pore size distributions during quartz precipitation in sandstone. Geochim Cosmochim Acta 2010;74:3539–52.
[14] Nagy KL, Lasaga AC. Simultaneous precipitation kinetics of kaolinite and gibbsite at 80C and pH 3. Geochim Cosmochim Acta 1993;57:4329–35.
[15] Kozeny J. Ueber kapillare Leitung des Wassers im Boden. Stizungsber Akad Wiss Wien 1927;136:271–306.
[16] Carman PC. Fluid flow through granular beds. Trans Inst Chem Eng 1937;15:150–67.
[17] Bernabe Y, Mok U, Evans B. Permeability–porosity relationships in rocks subjected to various evolution processes. Pure Appl Geophys 2003;160:937–60.
[18] Aharonov E, Tenthorey E, Scholz CH. Precipitation sealing and diagenesis 2. Theoretical analysis. J Geophys Res 1998;103:23969–81.
[19] Hoefner ML, Fogler HS. Pore evolution and channel formation during flow and reaction in porous media. AICHE J 1988;34:45–54.
[20] Algive L, Bekri S, Nader FH, Lerat O, Vizika O. Impact of diagenetic alterations on the petrophysical and multiphase flow properties of carbonate rocks using a reactive pore network modeling approach. Oil Gas Sci Technol 2012;67:147–60.
[21] Egermann P, Bekri S, Vizika O. An integrated approach to assess the petrophysical properties of rocks altered by rock-fluid interactions (CO_2 Injection). Petrophysics 2010;51:32–40.
[22] Caubit C, Hamon G, Sheppard AP, Oren PE. Evaluation of the reliability of prediction of petrophysical data through imagery and pore network modelling. Petrophysics 2009;50:32.
[23] Dupin HJ, Kitanidis PK, McCarty PL. Simulations of two-dimensional modeling of biomass aggregate growth in network models. Water Resour Res 2001;37:2981–94.
[24] De Boever E, Varloteaux C, Nader FH, Foubert A, Bekri S, Youssef S, et al. Quantification and prediction of the 3D pore network evolution in carbonate reservoir rocks. Oil Gas Sci Technol 2012;67:161–78.

[25] Algive L, Bekri S, Robin M, Vizika O. Reactive transport: experiments and pore-network modelling. In: International symposium of the society of core analysts, Calgary, Canada, 2007.
[26] Algive L, Bekri S, Vizika O. Reactive pore network modeling dedicated to the determination of the petrophysical property changes while injecting CO_2. In: SPE annual technical conference and exhibition. New Orleans, Louisiana: Society of Petroleum Engineers; 2009.
[27] Kang Q, Lichtner P, Viswanathan HS, Abdel-Fattah A. Pore scale modeling of reactive transport involved in geologic CO_2 sequestration. Transp Porous Media 2010;82:197–213.
[28] Mehmani Y, Sun T, Balhoff MT, Eichhubl P, Bryant S. Multiblock pore-scale modeling and upscaling of reactive transport: application to carbon sequestration. Transp Porous Media 2012;95:305–26.
[29] Raoof A, Hassanizadeh SM. A new method for generating pore-network models of porous media. Transp Porous Media 2010;81:391–407.
[30] Kim D, Peters CA, Lindquist WB. Upscaling geochemical reaction rates accompanying acidic CO_2-saturated brine flow in sandstone aquifers. Water Resour Res 2011;47.
[31] Li L, Peters CA, Celia MA. Upscaling geochemical reaction rates using pore-scale network modeling. Adv Water Resour 2006;29:1351–70.
[32] Arns JY, Robins V, Sheppard A, Sok R, Pinczewski WV, Knackstedt MA. Effect of network topology on relative permeability. Transp Porous Media 2004;55:21–46.
[33] Oren P, Bakke S. Reconstruction of Berea sandstone and pore-scale modelling of wettability effects. J Petrol Sci Eng 2003;39:177–99.
[34] Yanuka M, Dullien FAL, Elrick DE. Percolation processes and porous media: 1. Geometrical and topological model of porous media using a three-dimensional joint pore size distribution. J Colloid Interface Sci 1986;112:24–41.
[35] Koplik J, Lin C, Vermette M. Conductivity and permeability from microgeometry. J Appl Phys 1984;56:3127–31.
[36] Dullien FAL. Characterization of porous media – pore level. Transp Porous Media 1991;6:581–606.
[37] Fredrich JT, Menendez B, Wong T-F. Imaging the pore structure of geomaterials. Science 1995;268:276–9.
[38] Peters CA. Accessibilities of reactive minerals in consolidated sedimentary rock: an imaging study of three sandstones. Chem Geol 2009;265:198–208.
[39] Bakke S, Oren PE. 3-D pore scale modeling of sandstones and flow simulations in the pore networks. SPE J 1997;2:136–49.
[40] Okabe H, Blunt MJ. Prediction of permeability for porous media reconstructed using multiple-point statistics. Phys Rev E 2004;70:066135.
[41] Noiriel C, Luquot L, Made B, Raimbault L, Gouze P, van der Lee J. Changes in reactive surface area during limestone dissolution: an experimental and modelling study. Chem Geol 2009;00:160–70.
[42] Sheppard AP, Sok RM, Averdunk H. Techniques for image enhancement and segmentation of tomographic images of porous materials. Phys A 2004;339:145–51.
[43] Werth CJ, Zhang C, Brusseau ML, Oostrom M, Baumann T. A review of non-invasive imaging methods and applications in contaminant hydrogeology research. J Contam Hydrol 2010;00:1–24.
[44] Wildenschild D, Sheppard AP. X-ray imaging and analysis techniques for quantifying pore-scale structure and processes in subsurface porous medium systems. Adv Water Resour 2012;51:217–46.
[45] Sezgin M, Sankur B. Survey over image thresholding techniques and quantitative performance evaluation. J Electron Imaging 2004;13:146–65.
[46] Dong H, Blunt MJ. Pore-network extraction from micro-computerized-tomography images. Phys Rev E 2009;80:00.
[47] Porter ML, Wildenschild D. Image analysis algorithms for estimating porous media multiphase flow variables from computed microtomography data: a validation study. Comput Geosci 2010;14:15–30.
[48] Bhattad P, Willson CS, Thompson KE. Effect of network structure on characterization and flow modeling using X-ray micro-tomography images of granular and fibrous porous media. Transp Porous Media 2011;90:363–91.
[49] Jiang ZY, van Dijke MIJ, Wu K, Couples GD, Sorbie KS, Ma J. Stochastic pore network generation from 3D rock images. Transp Porous Media 2012;94:571–93.
[50] Oh W, Lindquist WB. Image thresholding by indicator kriging. IEEE Trans Pattern Anal 1999;21:00.
[51] Lindquist WB, Lee S-M, Coker DA, Jones KW, Spanne P. Medial axis analysis of three dimensional tomographic images of drill core samples. J Geophys Res 1996;101:8297–310.
[52] Lindquist WB, Venkatarangan A, Dunsmuir J, Wong T-F. Pore and throat size distributions measured from synchrotron X-ray tomographic images of Fontainebleau sandstones. J Geophys Res 2000;105:21509–27.
[53] Peng S, Hu Q, Dultz S, Zhang M. Using X-ray computed tomography in pore structure characterization for a Berea sandstone: resolution effect. J Hydrol 2012:254–61.
[54] Cnudde V, Boone M, Dewanckele J, Dierick M, Van Hoorebeke L, Jacobs P. 3D characterization of sandstone by means of X-ray computed tomography. Geosphere 2011;7:54–61.
[55] Pamukcu AS, Gualda GAR. Quantitative 3D petrography using X-ray tomography 2: combining information at various resolution. Geosphere 2010;6:775–81.
[56] CoreLab. Operations manual, profile permeameter PDPK-400. In: CL Instruments (Ed.). Houston, TX, 1996.
[57] Bear J. Dynamics of fluid in porous media. New York: Elsevier; 1972.
[58] Fetter CW. Applied hydrogeology. 4th ed. Upper Saddle River, New Jersey: Prentice Hall; 2001.
[59] Mavko G, Nur A. The effect of a percolation threshold in the Kozeny–Carman relation. Geophysics 1997;62:1480–2.